5
Synthesis, Structure and Antibacterial Property of Diorganotin Sulfide Assembled Using Intramolecular Coordination Approach

Research Article based on this study:

Mishra, A., Kumar, R., Khandelwal, A., Lama, P., Chhabra, M., and Metre, R. K., (2021), "Hemi Labile Intramolecular N → Sn Coordination in a Diorganotin (IV) Sulfide $[R_2Sn(\mu\text{-}S)]_2$ (R = 2-phenylazophenyl) Complex: Synthesis, Structure, DFT-NBO and Antibacterial Studies", *Polyhedron*, Vol.205, p.115302.

5.1 Introduction

Organotin compounds carry a major contribution in the area of main-group organometallic chemistry because of their diverse structures originating from metal's well expandable coordination modes and potential activity in catalytic and biologically driven applications [Da Silva et al., 2017; Hu et al., 2018; Murugavel et al., 2008; Tiekink, 1991]. Organostannoxanes are the prominent class of a broad family of organotin compounds, which includes organotin -oxides, -hydroxides, -carboxylates, -phosphates, -phosphonates etc. Based on the type of ligands, organotin precursor and reaction conditions, diverse, fascinating structures such as drum, ladder, prismane, football cage, butterfly, o-capped cluster, cube, double cube etc. have been isolated and structurally characterized to date [Chandrasekhar et al., 2002b].

Whereas other evolving class of organotin compounds consists of Sn-S unit in their structure. These compounds are generally obtained by use of various Sulphur based ligands such as sulfide (S^{2-}), thiols (RS^-), dithiocarbamates ($R_2NCS_2^-$), thiosemicarbazones {$RNC(NNR)S^-$}, thiophosphines ($R_2PS_2^-$), xanthates ($ROCS_2^-$), thiocarboxylates ($RCOS^-$) etc. However, unlike organostannoxane, literature shows that these compounds are relatively less explored. Sn-S units containing organotin compounds have recently been found to show remarkable electronic, photophysical, catalytic, and biological applications.
Recent literature reports on the rearrangement of NHC to abnormal NHC by an organotin sulfide cation [Wagner et al., 2013], a photon up-conversion of IR light into a broad white light spectrum using $[(RSn)_4S_6]$ (R = 4–$(CH_2$=$CH)$–C_6H_4) [Rosemann et al., 2016a], an interesting Zn metal trapping phenomenon by functionalizing the organotin sulfide cage [Geringer et al., 2020] and a molecular memory device based on organotin double-decker cage $[(RSn)_4S_6]$ (R=2-phenylazophenyl) with ON/OFF ratio 10^3 [Mishra et al., 2020] provides further evidence of their wide range of interesting properties. One of the hallmark properties of organotin compounds is their biological activity. Organotin compounds show their biological activity because of mainly two pathways; either by damaging the cell wall of the bacteria or by blocking the protein sites, i.e., inhibiting the growth of pathogenic bacteria [Hu et al., 2018]. In order to design new complexes in a way that enhances the antibacterial properties, understanding the mechanism is necessary. The biochemical properties are triggered by the electronic behavior of

the ligand attached to the metal center, coordination number, geometry of the metal center, the charge on the metal center etc [Shujah et al., 2018].

It has been observed in the literature that organotin complexes isolated with O, S or N donor multidentate ligands have displayed significant biological activity [Kapila et al., 2020; Md Yusof et al., 2020; Xing et al., 2020]. Antibacterial studies of Sn-S unit containing organotin complexes obtained from thiocarbohydrazone and dithiocarbamate ligands are known in the literature [Adeyemi et al., 2018, 2019a, 2019b; Zafarian et al., 2016]. Interestingly, a review report by Pellerito *et al.* emphasizes the biological potency of organotin complexes with Sn(IV) [Pellerito et al., 2002].

In the case of monoorganotin sulfides, two structural forms, namely adamantane and double-decker cage, are well known in the literature, while in the case of diorganotin sulfides, structural forms such as cyclic dimer $\{R_2Sn(\mu\text{-}S)\}_2$ and cyclic trimers $\{R_2Sn(\mu\text{-}S)\}_3$ are isolated depending on the bulkiness of substituent present on tin center [Lange et al., 2002; Mairychová et al., 2011; Mishra et al., 2020; Rosemann et al., 2016a]. However, to the best of our knowledge, molecular organotin sulfides have not been studied for their antibacterial behavior, unlike other class organotin compounds containing Sn-S units. Here in this chapter, we report the synthesis, structure, and antibacterial studies of a dinuclear diorganotin sulfide $[R_2Sn(\mu\text{-}S)]_2$ **(3)** obtained using 2-(phenylazo)phenyl as intramolecularly N→Sn coordinating substituent on the tin.

5.2 Experimental Section

5.2.1 Synthesis

$[R_2Sn(\mu\text{-}S)]_2$ (R = 2-phenylazophenyl) (3): To a clear solution of R_2SnCl_2 (R = 2-phenylazophenyl) (0.10 g, 0.18 mmol) in 20 ml of acetone/methanol (1:1), $Na_2S\cdot 9H_2O$ (0.043 g, 0.18 mmol) was added at once and stirred at room temperature for 8 hr. The suspension was filtered and precipitate was washed with water and hexane. The precipitate was dissolved in dichloromethane and X-ray quality crystals of **3** were grown by the slow diffusion of hexane into the dichloromethane solvent. Yield (Based on Sn): 0.075g (81%). M.P.>260ºC (decomp.); Elemental Analysis: Anal. Calcd for $C_{48}H_{36}N_8S_2Sn_2$: (1026.4) C, 56.17; H, 3.54; N, 10.92; S, 6.25. Found C, 56.36; H, 3.28; N, 10.57; S, 6.53. ^{1}H NMR (500MHz, $CDCl_3$, ppm): δ 8.45 (d), 7.8 (d), 7.45 (m), 7.38 (d), 7.18 (t), 5.3 (CH_2Cl_2), 1.54 (H_2O). $^{13}C\{^1H\}$NMR (125MHz, $CDCl_3$, ppm):δ 154, 150, 137, 136, 132, 130, 128, 127, 123. ^{119}Sn NMR (186.5MHz, $CDCl_3$, ppm): δ -125. ESI-MS: [**3**+H^+], 1027.062; IR (KBr, cm^{-1}): 3439 (br), 3058 (m), 2923 (w), 2844 (w), 1633 (w), 1577 (w), 1442 (m), 1296 (m), 1217 (m), 769 (s), 679 (s), 544 (m).

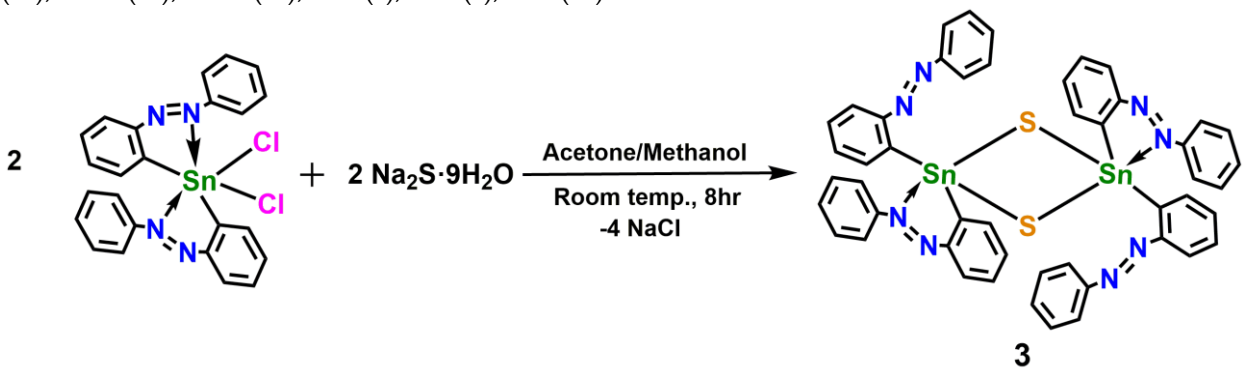

Scheme 5.1 Synthesis of complex **3**.

5.2.2 Single-Crystal X-ray Crystallography

The details pertaining to the data collection and refinement for **3** are given in Table 5.1.

Table 5.1 Crystal data and structure refinement parameters for complex **3**.

Identification code	**3**
Empirical formula	$C_{48}H_{36}N_8S_2Sn_2$

Formula weight	1026.35
Temperature/K	100(2)
Crystal system	monoclinic
Space group	$P2_1/n$
a/Å	15.329(7)
b/Å	10.173(4)
c/Å	15.570(7)
α/°	90
β/°	116.498(4)
γ/°	90
Volume/Å^3	2172.9(16)
Z	2
ρ_{calc}g/cm^3	1.569
μ/mm^{-1}	1.290
F(000)	1024.0
Crystal size/mm^3	0.250 × 0.180 × 0.120
Radiation	MoKα (λ = 0.71073)
2Θ range for data collection/°	3.1 to 49.982
Index ranges	-18 ≤ h ≤ 18, -12 ≤ k ≤ 12, -18 ≤ l ≤ 18
Reflections collected	45409
Independent reflections	3822 [R_{int} = 0.0253, R_{sigma} = 0.0109]
Data/restraints/parameters	3822/0/271
Goodness-of-fit on F^2	1.085
Final R indexes [I>=2σ (I)]	R_1 = 0.0233, wR_2 = 0.0542
Final R indexes [all data]	R1 = 0.0255, wR2 = 0.0560
Largest diff. peak/hole / e Å^{-3}	1.51/-0.59

5.2.3 Assessment of Antibacterial Activity

The potential of complex **3** for inhibiting the bacterial activity was assessed by employing Kirby-Bauer standard disc diffusion method [Zafarian et al., 2016]. For this, three concentrations of the complex were taken, including 10, 15 & 20 mg/ml, using chloroform as a solvent and these were coated on glass discs with the help of a spin-coater. The glass slides were autoclaved prior to the coating. The glass discs were then exposed to the hot air gun for 5 min. in order to remove any traces of chloroform. Further, the antibacterial activity of complex **3** was determined against both gram-positive bacteria *Micrococcus luteus* and gram-negative bacteria *Escherichia coli*. The LB media with 2% agar was used to lawn culture the bacterial suspension equivalent to 0.5 McFarland, followed by placing discs on these cultures. The plates were then incubated at 37°C for 24 h. For comparison, some standard antibiotics, namely ampicillin and kanamycin, were also tested for antibacterial activity. The zone of inhibition exhibited by complex **3** as well as antibiotics was measured for further analysis.

5.2.4 Theoretical Calculations

The density functional theory (DFT) and time-dependent DFT (TDDFT) calculations were carried out using Gaussian 09 (Revision D.01) [Frisch et al., 2009] suite of program and ORCA 4.0.1 program [Neese, 2012]. The complex **3** geometry was optimized using TPSSh functional [Dirac, 1929; Perdew et al., 2018; Slater, 1951; Staroverov et al., 2003; Tao et al., 2003] with def2-SVP basis set (TPSSh/def2-SVP) for all the atoms. The single point energy calculation with a higher basis set has been performed on the optimized geometry coordinates using def2-TZVP basis set [Weigend et al., 2005]. On the DFT optimized geometry of complex **3,** the TDDFT calculations using ORCA 4.0.1 program have been done with TPSSH/def2-TZVP basis set and

RIJCOSX approximation [Neese, 2012]. The solvent effect was considered using CPCM method with DCM. The quantitative analysis of the shape of the metal centers of complex **3** has been analyzed using SHAPE2.1 program [Llunell et al., 2013]. The NPA charges, WBIs and NBO analysis have been performed at the same level of theory (TPSSh/def2-TZVP//TPSSh/def2-SVP) using NBO program (version 3.1) implemented in Gaussian 09RevD.01 [Foster, 2006; Glendening et al., 2003]. The visualization of molecular orbitals has been done using Chemcraft programs [Zhurko et al., 2009].

5.3 Results and Discussion

5.3.1 Synthetic Aspects

Complex **3** is synthesized by the reaction of intramolecularly N→Sn coordinated diorganotin precursor R_2SnCl_2 (R= 2-(phenylazo)phenyl) with $Na_2S{\cdot}9H_2O$ in the stoichiometric ratio in acetone/methanol mixture at room temperature (Scheme 5.1). The crystal structure of Complex **3** shows the presence of two identical Sn atoms in distorted trigonal bipyramidal geometry. A single resonance was observed at δ -125 ppm in ^{119}Sn NMR spectrum, indicating both the Sn atoms of **3** to be in the same chemical environment (Fig. 5.1). ESI-MS studies of **3** reveal the presence of molecular ion peak **3**+H^+ at m/z 1027.062. Thermogravimetric analysis revealed that complex **3** is stable up to 280°C and undergoes single-step decomposition. At 600°C, the decomposed residue was found to be 50% (Fig. 5.2).

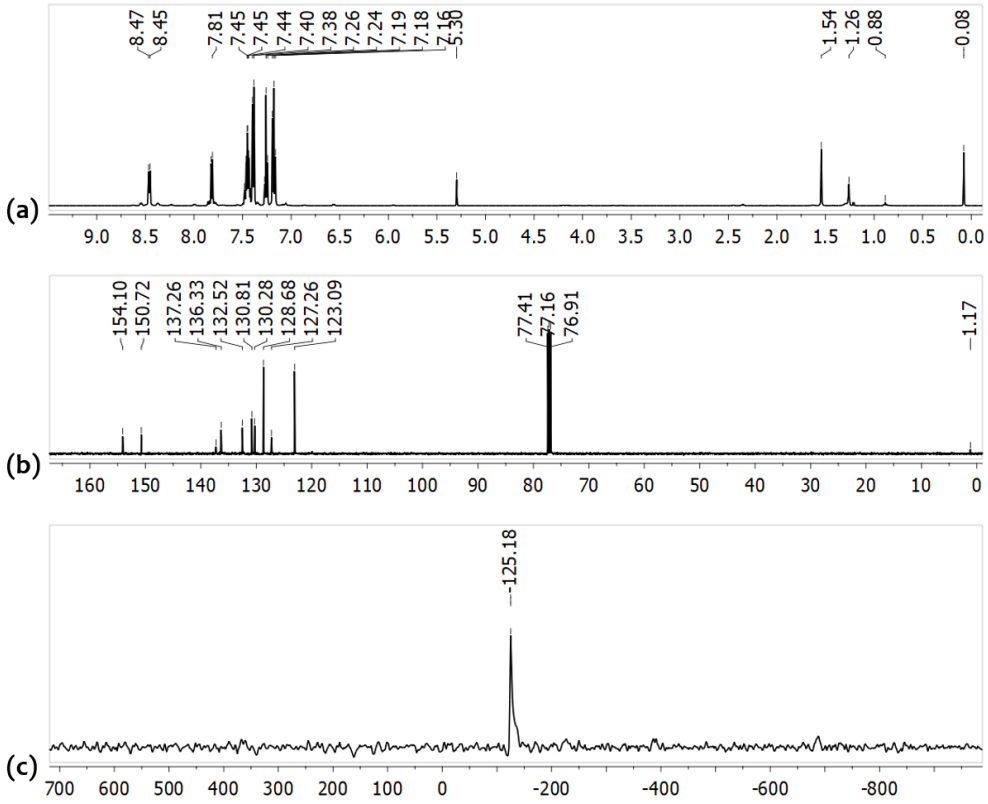

Fig. 5.1 (a) ^{1}H NMR, **(b)** ^{13}C NMR and **(c)** ^{119}Sn NMR of complex **3** recorded in $CDCl_3$.

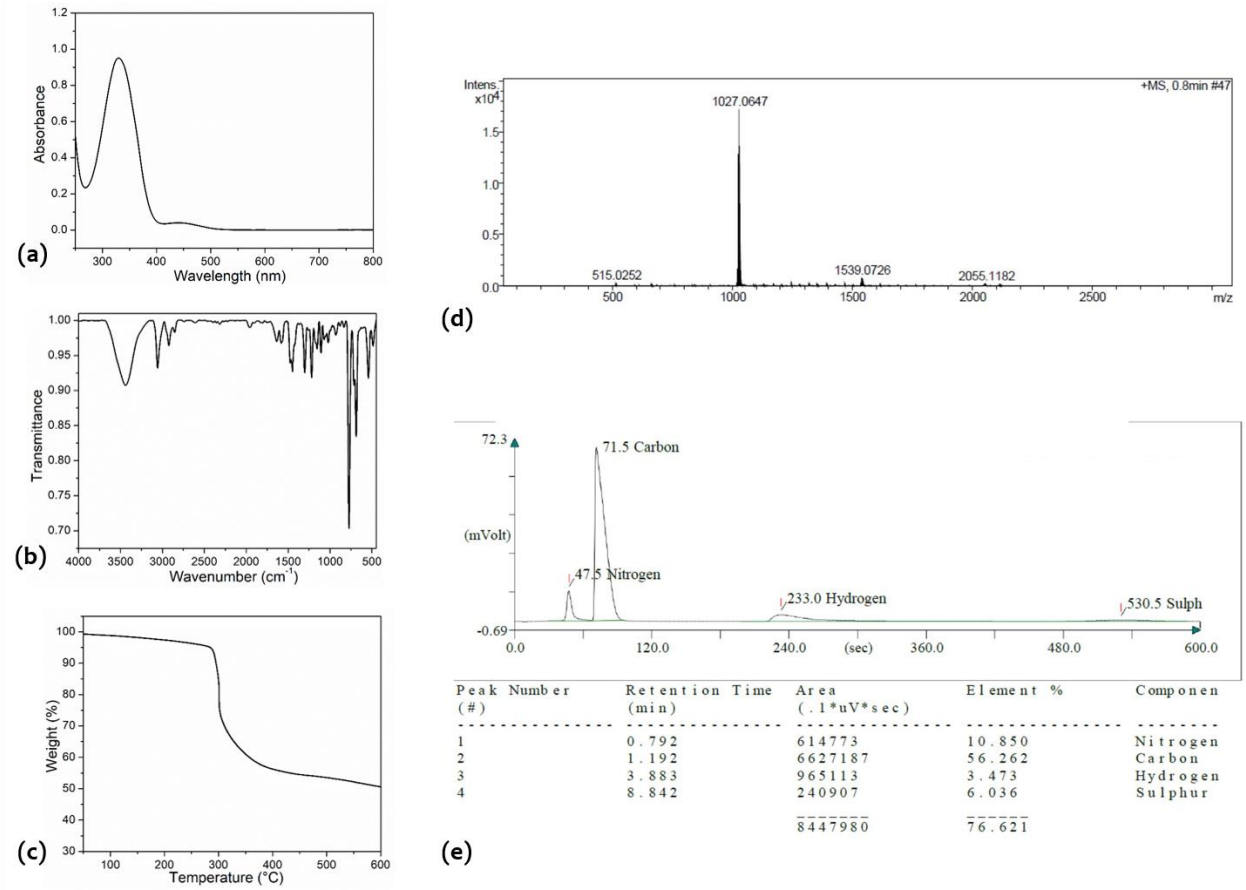

Fig.e 5.2 (a) UV-Vis spectrum (conc. 10^{-5}M in $CHCl_3$), **(b)** FTIR spectrum, **(c)** TGA (under N_2 atmosphere) **(d)** ESI-MS spectrum and **(e)** CHN analysis of complex **3**.

5.3.2 Molecular and Supramolecular Structure of Complex 3

The molecular structure of complex **3** is shown in Fig. 5.3(a). Complex **3** consists of two crystallographically unique asymmetric units R_2SnS (R = 2-(phenylazo)phenyl). Structurally, it is a centrosymmetric dimer with a four-membered Sn_2S_2 ring. Both the Sn atoms (Sn1 and Sn1′) are bridged by two μ-S^{2-} ligands. Closer inspection of the crystal structure of **3** reveals the preservation of only one N→Sn intramolecular coordination on the Sn center, indicating the hemi labile nature of N→Sn intramolecular coordination present in R_2SnCl_2. Such hemi labile nature of intramolecular coordination has been previously observed for organostannoxanes obtained using monoorganotin precursor $RSnCl_3$ [Metre et al., 2014]. The N→Sn distance in **3** (2.6335 Å) is observed to be slightly larger than that in the starting precursor; the N→Sn average is 2.55 Å [Briansó et al., 1983]. It has a well-established planar Sn_2S_2 core [Fig. 5.3(b)], but the Sn-S distances of the ring are found to be slightly different, which can be attributed to N→Sn intramolecular coordination. N2 center being the Lewis base when attacks on Lewis acidic Sn1 center over the face C1C13S1, the axial Sn1-S1′ distance gets elongated in comparison to axial Sn1-S1 [Fig. 5.3(c)]. Complex **3** has a Sn_2S_2 ring with Sn1-S1, 2.4007 Å and Sn1-S1′, 2.4761 Å, which are in close agreement with the previous reports on $[R_2Sn(\mu\text{-}S)]_2$ bearing N→Sn intramolecular coordination [Jurkschat et al., 1992]. And also, these bond parameters are much closer to the four-membered Sn_2S_2 ring (Sn-S, 2.4001, 2.4817 Å and Sn-S-Sn, 86.79°) of our previously reported tetranuclear double-decker $[(RSn)_4(\mu\text{-}S)_6]$ (R=2-phenylazophenyl) [Mishra et al., 2020]. Each Sn center in **3** is pentacoordinated [S1, S1′, C1, C13 and N2], possessing distorted trigonal bipyramidal geometry keeping S1′ and N2 at axial position.

The geometrical symmetry of Sn center can be expressed in terms of Addison's Tau parameter (τ). In case of complex **3**, it is found to be τ=0.68 (τ=1 for perfect trigonal bipyramidal geometry) for the Sn center [Addison et al., 1984; Mishra et al., 2020].

Single-crystal growth of complex **3** is accompanied by the formation of various supramolecular architectures in the solid-state such as 1D chain and 2D plane-like assembly

owing to the presence of hydrogen bonding C-H…N, C-H…S, π…π and C-H…π non-covalent interactions. (Fig. 5.4) [Metre et al., 2014; Mishra et al., 2020, 2021b, 2021d].

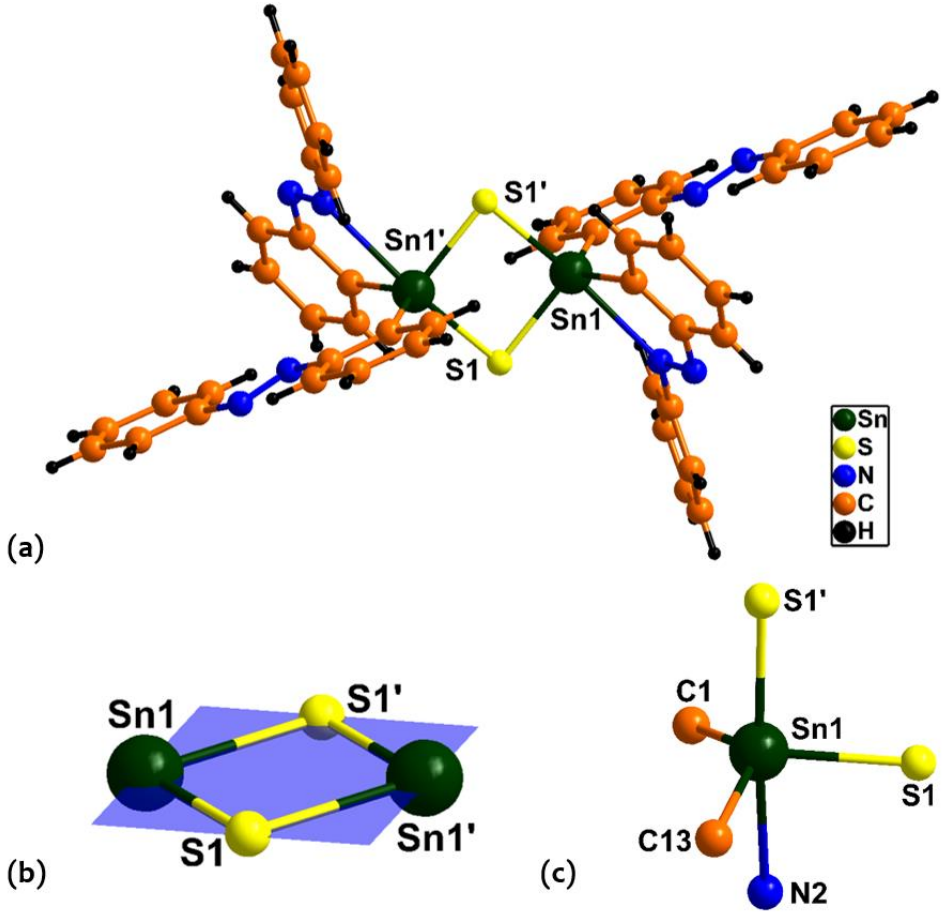

Fig. 5.3 (a) Molecular structure of complex **3**; Bond distance (Å) and bond angle (°) parameters: Sn1'-S1', 2.4007(1) Å; Sn1'-S1, 2.4761(1) Å; Sn1-S1-Sn1', 85.907(3)°; Sn1-S1'-Sn1', 85.907(3)°, S1-Sn1-S1', 94.093(3)°; **(b)** Core structure with a molecular plane; **(c)** Coordination environment of Sn in complex **3**; Sn1-S1, 2.4007(1) Å; Sn1-S1', 2.4761(1) Å; Sn1-N2, 2.6335(2) Å; Sn1-C1, 2.1365(2) Å; Sn1-C13, 2.1306(3) Å; N2-Sn1-S1', 167.175(5)°; N2-Sn1-S1, 82.547(5)°, C1-Sn1-C13, 126.094(1)°; C1-Sn1-S1, 115.586(7)°.

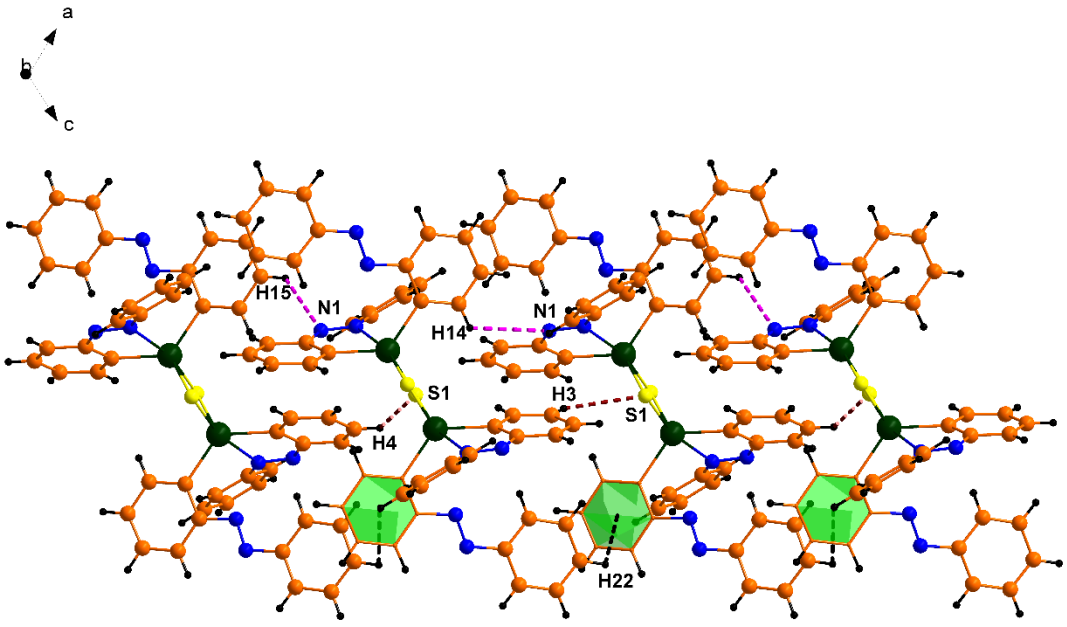

(a)

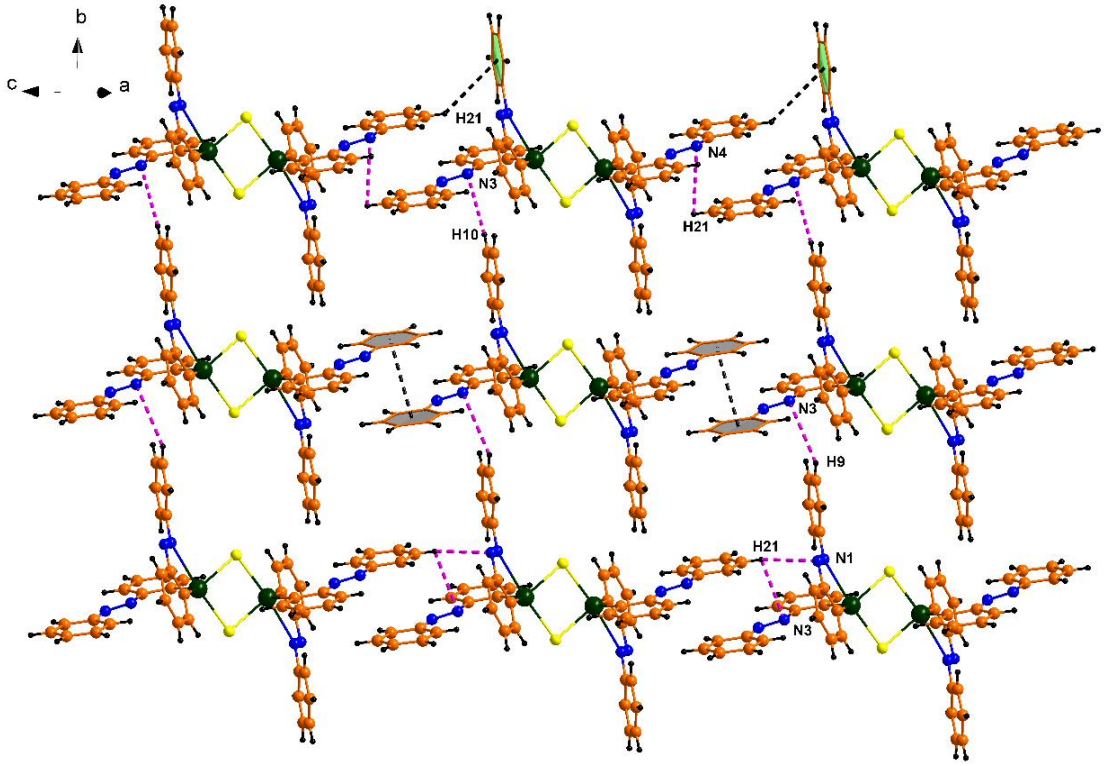

(b)

Fig. 5.4 (a) One-dimensional supramolecular assembly of **3** formed by CH…π, CH…S, CH…N interactions. Metric parameters are as follows; H22-π, 3.4881(1) Å; H3-S1, 3.0710(1) Å; H4-S1, 3.2938(1) Å; H14-N1, 3.4615(2) Å; H15-N1, 3.0605(2) Å. **(b)** Two-dimensional supramolecular architecture of **3** formed by CH…π, π…π, CH…N interactions. Metric parameters are as follows; H21-π, 3.6737(1) Å; π…π, 3.9903(1) Å; H10-N3, 3.0460(2) Å; H21-N4, 3.3569(2) Å; H9-N3, 3.4469(3) Å; H21-N1, 2.9805(3) Å; H21-N3, 3.1785(2) Å.

5.3.3 Photophysical Studies

Theoretical studies were performed in collaboration. The absorption spectrum of complex **3** was obtained at room temperature in Dichloromethane (DCM) solvent, keeping the concentration of 10^{-5} M. Two bands were observed in the absorption spectrum, one broad and intense band at 330 nm whereas another broad and weak band at 450 nm. The intense band is attributed to the $\pi \rightarrow \pi^*$ spin allowed transition of 2-phenylazophenyl, while the weak band is attributed to the $n \rightarrow \pi^*$ the spin forbidden transition [Mishra et al., 2020]. To understand these peaks, we have performed the time-dependent density functional theory (TDDFT) analysis [Neese, 2012].

The TDDFT computed peaks are in well agreement with the experimental peaks, such that the intense peak at 336 nm is very close to the experimental peak at 330 nm and this peak is due to spin allowed $\pi \rightarrow \pi^*$ transition (see Fig. 5.5) and there is a possibility of mixing this peak with other peaks at 363 nm and 406 nm which consists of mixed $n+\pi \rightarrow \pi^*$ transitions. The lowest intensity peak at 482 nm is slightly upshifted (experiment 450 nm) but is within the error limit of DFT. Here, a spin-forbidden $n \rightarrow \pi^*$ transition takes place, which is predicted previously. The prominent ligand-to-ligand transitions are present in this complex.

- **Computational Studies**

To understand the electronic structure of complex **3**, the density functional theory (DFT) studies were performed using Gaussian 09 (Revision D.01) suite of program [Frisch et al., 2009]. The optimized geometry parameters of complex **3** reveal that the coordination environment around both the Sn centers is the same. Shape analysis using the program SHAPE 2.1 has been performed to understand the geometry around the Sn center [Llunell et al., 2013]. This reveals that the geometry around the Sn center is trigonal bipyramidal (TBP) with a slight deviation of 2.061.

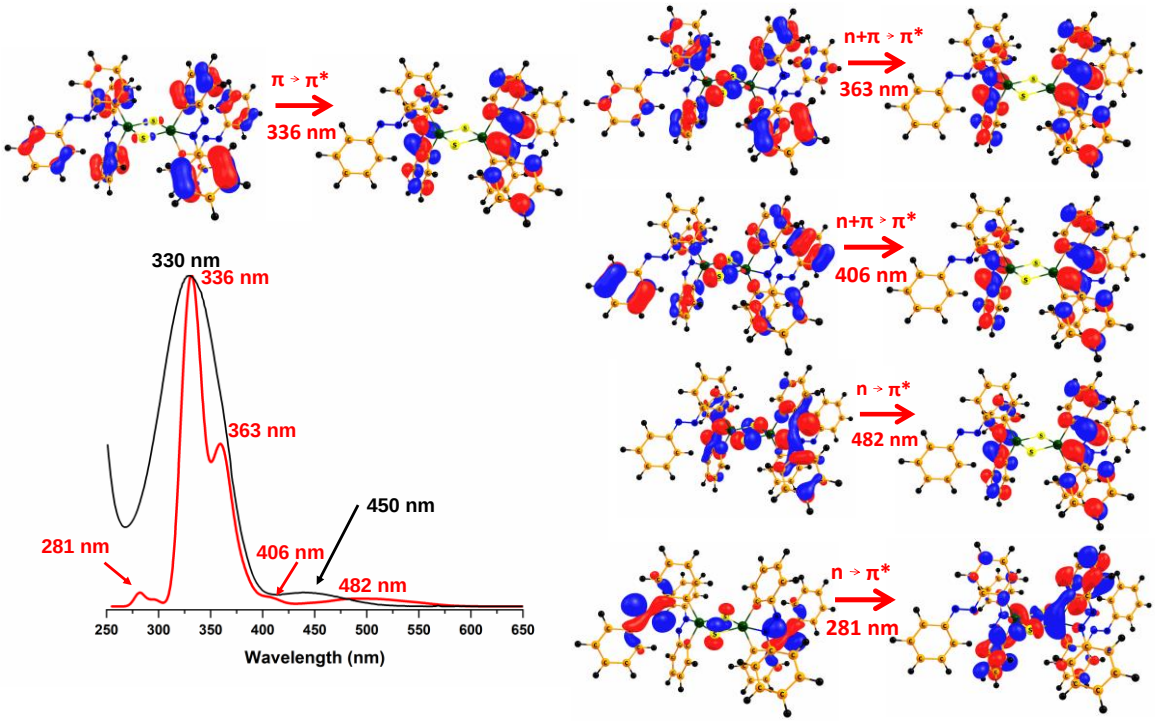

Fig. 5.5 DFT-computed absorption spectra (in red) of complex **3** using TD-DFT calculations and its corresponding orbitals involved in the transitions. The experimental spectrum of **3** is given in the black line for comparison.

To understand the bonding picture of complex **3**, the natural bond orbital **(**NBO) analysis was performed. As mentioned previously that both Sn are equivalent, so the involvement of bonding orbitals is also the same for these metal centers. Here, each penta-coordinated Sn has two types of Sn-S (Sn1-S1, and Sn1-S1′), two types Sn-C (Sn1-C1 and Sn1-C13) and one type of Sn-N (Sn1-N2). As the Wiberg bond index (WBI) suggests the strength of the particular bond, here, the WBI for the Sn1-N2 bond is 0.1849, which is the lowest among all, which means this bond is the weakest bond among all the five bonds of Sn metal (see Table 5.2). For a similar type of atoms bond, the WBI strength is inversely proportional to bond length (see Table 5.2).

Table 5.2 B3LYP-computed bond lengths and their corresponding Wiberg bond index (WBI) around Sn1 center.

Parameter	*Bond length (Å)*	*WBI*
Sn1-S1	2.437	0.8134
Sn1-S1'	2.525	0.6632
Sn1-C1	2.160	0.6929
Sn1-C13	2.165	0.6777
Sn1-N2	2.601	0.1849

Through the natural population analysis (NPA), it was found that the charge on Sn is +1.518, which is in good agreement with the formal oxidation state of Sn^{IV} [Eußner et al., 2014]. Similarly, for the coordinated atoms, the NPA charges are in well agreement with the formal oxidation state (see Table 5.3).

Table 5.3 The Natural population analysis (NPA) charges on metals and coordinated atoms.

Atom	*Formal Oxidation State*	*NPA Charges*
Sn1	+IV	+1.518
C1/C13	-I	-0.386/-0.356
S1/S1'	-II	-0.802
N2	0	-0.166

The analysis of the NBO plot reveals that the Sn1-C1, Sn1-C13 and Sn1-S2 bonds in Sn^{IV} coordination environment have ~71% contribution from coordinated ligands atoms and ~29% from Sn atom (see Fig. 5.6), which indicates the ionic nature in these bonds. With the careful observation of orbital pictures, it was found that these three bonds are formed due to the overlapping between sp^2-hybrid orbitals (s, p_x and p_y) of Sn with the p-orbitals of 2-(phenylazo)phenyl carbons (C1 and C13), S1 (sulfide ligands). Here, two dative (coordinate) bonds N2(LP)→Sn1(LP*) and S1′(LP)→Sn1(LP*) are formed by the donation of lone pair (LP) electrons of nitrogen and sulfur to empty antibonding lone pair (LP*) formed with pd-hybrid orbitals (p_z and d_{z^2}) (see Fig. 5.6). These two prominent donor-acceptor interactions' second-order stabilization energies are 31.07 kcal/mol for N2→Sn1 and 179.04 kcal/mol for S1′→Sn1 (see Table 5.4). These observations are in accord with the ideal TBP geometry for Sn^{IV} center.

Table 5.4 The second-order perturbation analysis of donor (i) and accepter (j) orbital with their stabilization energies (E_2) (in kcal/mol).

Donor (i)	*Acceptor (j)*	*Stabilization Energy (E_2)*
LP S1'	LP* Sn1	179.04
LP N2	LP* Sn1	31.07

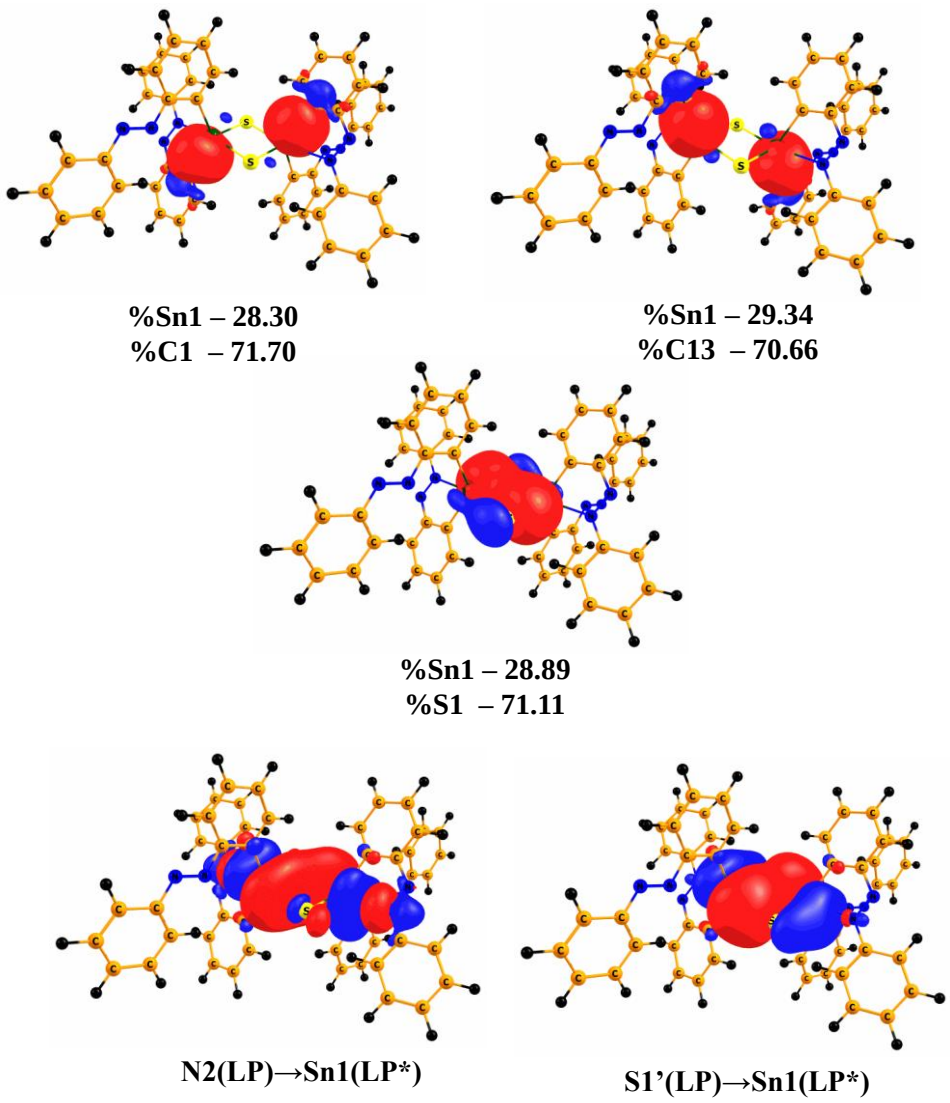

Fig. 5.6 Natural bonding orbital (NBO) diagram for the Sn^{IV}-coordinated environment of complex **3**. The contour value used to generate the plots are 0.03 a.u.

As the nature of highest occupied (HOMO) and lowest unoccupied (LUMO) molecular orbitals are important to predict the various properties of molecules. The HOMO and LUMO

energies and their gap were computed for complex **3**. The energy of the HOMO orbital is found to be -6.0 eV and the molecular orbital geometry reveals that it is mainly located on the sulfur atoms. From the previous literature, it is known that sulfur-containing complexes show good biological activity, such as antibacterial and antimicrobial (see Fig. 5.7) [Adeyemi et al., 2018; Cui et al., 2019; Müller et al., 1981; Soliman et al., 2016]. The LUMO energy is found to be -3.2 eV and the molecular orbital geometry consists of mainly π^*-orbital of 2-phenylazophenyl ligands (see Fig. 5.7). The HOMO-LUMO gap is found to be 2.8 eV, which is within the range of previously reported bioactive molecules [Cui et al., 2019; Kumari et al., 2019; Soliman et al., 2016].

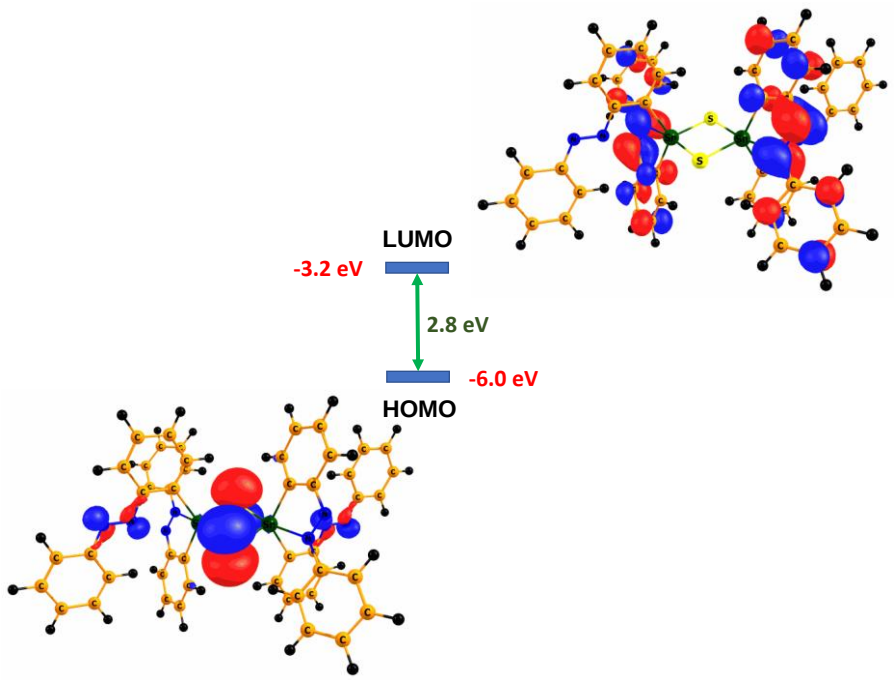

Fig. 5.7 DFT-computed HOMO-LUMO energies, gap and their corresponding molecular orbital diagram of complex **3**. The contour value used to generate the plots are 0.03 a.u.

5.3.4 Antibacterial Studies

The antibacterial activity of complex **3** was investigated in collaboration. Standard antibiotics such as ampicillin and kanamycin were also taken into account as a positive control. Both gram-negative (*Escherichia coli*) and positive (*Micrococcus luteus*) bacteria were included in the study. Table 5.5 summarizes the data obtained from antibacterial studies. The antibacterial potential of organotin complexes can be described by Overton's concept and Tweedy's chelation theory. Overton's concept postulates the role of lipophilicity of complexes towards antimicrobial activity. The lipid-soluble complexes can easily invade the outer lipid bilayer of microorganisms, therefore disrupting the cellular organization [Adeyemi et al., 2019a]. On the other hand, according to Tweedy's chelation theory, the complexation leads to the reduction of the central metal ion's polarity due to the partial distribution of positive charge among other donor moieties of the complex. In addition to this, the pi electron delocalization over the chelating can also increase the lipophilic nature of the central tin atom [Roy et al., 2016]. This enhanced lipophilicity of the central tin atom allows penetration of complex into the cell membrane. Here, in this molecule, the central tin atom is associated with sulfur which is a donor group, lowering the polarity of the central atom tin. The decreased polarity and pi-electron delocalization collectively led to enhanced lipophilicity and permeability of complex into cell membrane. Once the complex enters the cell membrane, it disrupts the lipid-protein organization of cell, resulting in inhibition of cellular metabolism and growth. Previous studies have also confirmed the role of the Sn-S bond towards antimicrobial activity in organotin (IV) complexes. Complex **3** exhibited comparable antibacterial activity against gram-positive as well as gram-negative strains. There was no significant difference observed in the zone of inhibition (ZOI) obtained for *M. luteus* with all the three concentrations employed in the study (Fig. 5.8). On the other hand, complex **3** showed a bit compromised antibacterial activity towards the

culture of *E. coli* (Table 5.5). *E. coli* is a gram-negative bacteria which possesses an outer lipid membrane composed of lipopolysaccharide membrane, making it less susceptible to antibiotic agents. This membrane blocks the entry of complexes into the bacterial cells, resulting in lesser or no activity. However, the results obtained in this study clearly demonstrate that complex **3** is equally effective against both gram-positive and negative bacteria (Fig. 5.8).

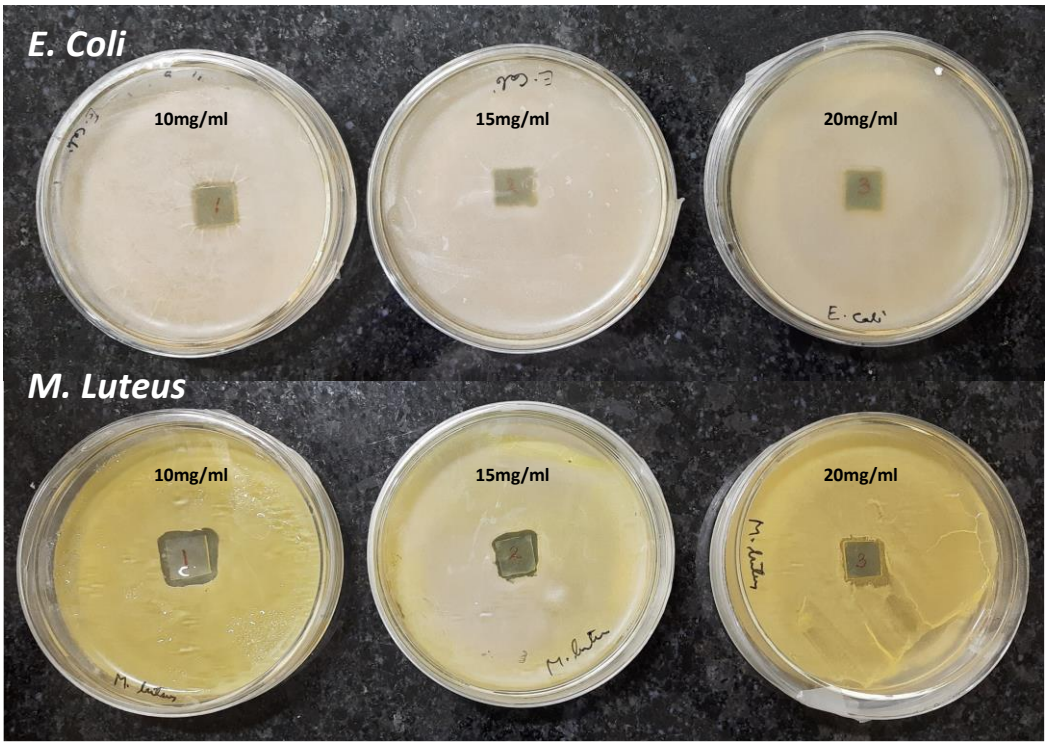

Fig. 5.8 Inhibition zones of Complex **3** against E. coli and M. Luteus.

Table 5.5 Inhibition zone of the complex **3** and the antibiotic agents.

S. No.	*Antibacterial materials*	*Concentration (mg/ml)*	*Zone of inhibition (mm)*	
			M. luteus	*E. coli*
1.	Complex **3**	10	9	6
2.	Complex **3**	15	6	NS
3.	Complex **3**	20	6	NS
4.	Ampicillin	0.1	NS	4
5.	Kanamycin	0.05	NS	6

5.4 Conclusion

Herein, we report the synthesis of intramolecularly N→Sn coordinated dinuclear diorganotin sulfide complex $[R_2Sn(\mu\text{-}S)]_2$ (R = 2-phenylazophenyl) (**3**). The molecular structure of **3** is determined with single-crystal x-ray crystallography. Complex **3** exhibits cyclic dimeric ring structure with the retention of partial intramolecular N→Sn coordination, indicating the hemi-labile nature of N→Sn intramolecular coordination present in R_2SnCl_2. Here, the TDDFT calculation shows that complex **3** mostly has π→π* and n→π* ligand-to-ligand transitions. The electronic structure analysis suggests that the coordination environment around both the Sn atoms are equivalent and the metal-coordinated bonds are ionic in nature (NBO analysis). The HOMO-LUMO gap of this complex is found to be 2.8 eV and HOMO is located on sulfur atoms while LUMO is on 2-phenylazophenyl ligands. As sulfur-containing complexes show good bioactivity and this complex contains sulfur-based HOMO, which created an interest in exploring the biological activity of this complex. Furthermore, complex **3** was turned out to be equally effective against the gram-positive bacteria as well as gram-negative strains.